JOM, Vol. 68, No. 4, 2016
DOI: 10.1007/s11837-016-1838-9

Microstructural and Photoacoustic Infrared Spectroscopic Studies of Human Cortical Bone with Osteogenesis Imperfecta

CHUNJU GU,[1,2] DINESH R. KATTI,[1,3] and KALPANA S. KATTI[1,4]

1.—Department of Civil and Environmental Engineering, North Dakota State University, Fargo, ND 58105, USA. 2.—e-mail: chunju.gu@ndsu.edu. 3.—e-mail: dinesh.katti@ndsu.edu. 4.—e-mail: Kalpana.Katti@ndsu.edu

The molecular basis of bone disease osteogenesis imperfecta (OI) and the mineralization of hydroxyapatite in OI bone have been of significant research interest. To further investigate the mechanism of OI disease and bone mineralization, Fourier transform infrared spectroscopy (FTIR), scanning electron microscopy, and x-ray diffraction (XRD) are used in the present study to describe the structural and compositional differences between OI and healthy bone. OI bone exhibits more porous, fibrous features, abnormal collagen fibrils, and abnormal mineral deposits. Likewise, photoacoustic-FTIR experiments indicate an aberrant collagen structure and an altered mineral structure in OI. In contrast, there is neither significant difference in the non-collagenous proteins (NCPs) composition observed nor apparent change in the crystal structure between OI and healthy bone minerals as shown in XRD and energy-dispersive x-ray spectroscopy (EDS) results. This observation indicates that the biomineralization process is more controlled by the bone cells and non-collagenous phosphorylated proteins. The present study also confirms that there is an orientational influence on the stoichiometry of the mineral in OI bone. Also, a larger volume of the hydrated layer in the transverse plane than the longitudinal plane of the mineral crystal structure is proposed. The appearance of a new C–S band in the FTIR spectra in OI bone suggests the substitution of glycine by cysteine in collagen molecules or/and an increased amount of cysteine-rich osteonectin that relates to mineral nucleation and mineral crystal formation.

INTRODUCTION

Osteogenesis imperfecta (OI) is an inheritable disease characterized by the fragility of bones and other tissues rich in the type I collagen.[1–3] About 90% of OI cases are due to a causative variant in one of the two structural genes (COL1A1 or COL1A2) for the type I procollagens. OI provides an interesting platform for investigating how alterations of collagen at the molecular level cause changes in the structure of bone. The severity of the disease varies ranging from very mild forms without fractures to intrauterine fractures and perinatal lethality. These mutations range in complexity from simple deletions, insertions, and single base substitutions that convert a codon for glycine to a codon for a bulkier amino acid preventing proper folding of the triple helix of collagen. Among the 1277 mutations found, over 85% are substitutions.

Various experiments have been conducted to examine the influence of collagen defects on different constituents of bone, the structural characteristics of bone, and cell activities. The resulting findings help reveal the mechanisms of OI disease. As a direct effect of the mutations in the procollagen, it has been found that the amount of collagen from OI bone is less than that from age-matched normal controls,[4] collagen aggregation is abnormal,[5] stabilizing intermolecular cross-links are reduced,[6] and the diameter of type I collagen fibrils in OI bone is altered[7,8] as compared with normal bone. As an indirect effect from the mutations in the procollagens, other organic matrix proteins can also exhibit an abnormal expression pattern.[9–11] Also, higher mineral/matrix ratios and lower carbonate: mineral ratios are usually seen in the mouse model of osteogenesis imperfecta.[12–14] Lower Ca/P ratio is also seen in OI human patients.[15] Increased bone turnover is also observed in children and mice with OI,[16–18] whereas reduced bone turnover is seen in some OI (type I, and IV) adults and children.[19,20] Further, cell activities are influenced by the defective procollagen as an increase in the number of vascular channels,[1,21] and increased osteoclasts and osteocytes are seen in OI bone.[22] Meanwhile, deposition of new bone at the single osteoblast level is reduced and is not compensated by the increased osteoblast cell number.[17,23,24] Modulus mapping experiments have indicated spatial variation of elastic moduli consistent with the distribution of mineralized fibril and extrafibrillar mineral in OI bone.[25] In addition, molecular and nanomechanical changes are observed in different anatomical positions for cross-sections of OI.[26]

It is suggested that the increased remodeling in OI (increased number of osteoclasts and osteocytes) can result from increased microdamage in the bone matrix,[17] and the occurrence of the microdamage might be caused by higher mineralization.[27] Increased nucleation centers create a higher mineralization density in OI bone matrix.[23] Therefore, Roschger et al. attributed the OI phenotype to a failure in the osteoblast differentiation pathway and concomitant synthesis of noncollagenous matrix protein that disturbs bone matrix stoichiometry, and this failure results in similar bone mineralization conditions in different OI types.[23] In other studies, it is also suggested that the low ultimate strength observed in *oim*/*oim* bone despite its high mineralization content results from defective mineral in *oim*/*oim* bone causing prohibition of normal fusion of crystals into an end-to-end fusion of contiguous structures.[28] Also, the structural changes in the mineral result from an abnormal collagen fibril scaffold for mineral deposition.[28]

Numerous infrared studies have been conducted on OI bone, and four items have usually been selected as standards to describe the composition and mineral crystal of bone: (1) mineral/matrix ratio [calculated from the integrated areas of phosphate (916–1180 cm^{-1}) to amide I (1592–1712 cm^{-1})], (2) collagen cross-linking network maturity (Cross Link Ratio (XLR), the peak intensity ratio of amide I subbands at 1660 cm^{-1} and 1690 cm^{-1}), (3) carbonate/phosphate ratio [calculated as the integrated area of the $v2$ carbonate peak (840–892 cm^{-1}) to that of the phosphate], and (4) crystallinity (XST, calculated as the phosphate sub-band 1030 cm^{-1}/1020 cm^{-1} peak intensity ratio 1030 cm^{-1}/1020 cm^{-1}). These studies on human osteogenesis imperfections suggest that significantly increased mineral/matrix ratios in both cortical and trabecular bone of two high BMD OI patients is observed as compared with normal or classical OI bone.[29] Fourier transform infrared spectroscopy (FTIR) has been conducted on different clinical types (I, IB, and IVA) of OI patients.[15] FTIR studies of OI mouse models suggest that *Fro*/*fro* and *oim*/*oim* genotypes exhibit abnormal collagen cross-linking as determined by FTIR[14] and higher mineral/matrix ratios and lower carbonate/phosphate ratios for *oim*/*oim* as compared with normal controls are observed.[12,13,28,30] Further, in the *oim*/*oim* mouse model, the bisphosphonate treatment results in increased metaphyseal bone mineralization, but does not improve mineral maturity.[31] In addition, in recent publications, acid phosphate content HPO_4^{2-} (1128 cm^{-1}/1096 cm^{-1}) has been utilized to estimate the amount of acid phosphate substitution in the mineral lattice and increased acid phosphate contest was noted in Brtl/ + teeth.[32,33] Since bone is an orthotropic material, the orientational difference in the stoichiometry of hydroxyapatite was investigated using FTIR in our previous study.[34] This orientational difference was found to be influenced by the interactions between the collagen molecules and mineral. In the present study, the stoichiometry of hydroxyapatite from both transverse and longitudinal planes is examined using FTIR, x-ray diffraction (XRD), and energy-dispersive x-ray spectroscopy (EDS).

OI cortical bone (putative type I) was selected in the present study to compare with healthy cortical bone. It is to be noted that the availability of healthy and diseased bone samples of similar age, and gender is highly limited and perhaps needs to be addressed in the biomedical forums. This study presented on the limited samples is still suggestive of the differences between healthy and OI. Earlier, we have reported that the OI bone shows similar viscoelastic response as the normal bone[25] and nanomechanical differences in various anatomical positions of bone crossections were reported.[26] In this work, the ultrastructure, molecular differences, and mineral crystal structure as well as Ca/P ratio were studied with the techniques of field emission scanning electron microscopy (FESEM), FTIR, XRD, and EDS.

MATERIALS AND METHODS

Materials

Human normal cortical bone (femur, no apparent metabolic bone disease record, 27 years old, female) and OI cortical bone (tibia, no apparent metabolic bone disease record, 22 years old, female with pregnancy experience) were both obtained from the National Disease Research Interchange (NDRI), PA, USA, and were stored in a freezer at −70°C. The OI type is putative type I, the mildest type, since the patient height was 170.2 cm, and weight 81.6 kg. Genetic analysis was not undertaken for these samples but the sample source at NDRI has labeled these samples as having OI through clinical diagnosis which is done on the basis of genetic analysis for the patient.

A 20-mm-thick transverse section was obtained from the mid-diaphysis of the cortical bone with a diamond saw. Marrow and flesh were then removed using a ceramic knife. Further, the bone was washed with deionized (DI) water at room temperature for approximately 10 min to avoid deterioration of the bone, following which it was further trimmed down using a low-speed diamond-wafering blade (Buehler; Isomet, Lake Bluff, IL, USA) to obtain specimens with a thickness of about 1 mm from both transverse and longitudinal planes from anterior sections (Fig. 1). These specimens were then ready for photoacoustic-FTIR (PA-FTIR) and XRD characterizations.

Scanning Electron Microscopy

The microstructure of the bone specimens was examined using a JEOL JSM-7600F analytical high-resolution FESEM (JEOL, Peabody, MA, USA). Sample preparation for the scanning electron microscope (SEM) imaging involved fixing in 2.5% glutaradehyde (Tousimis) overnight followed by rinsing twice with sodium phosphate buffer (0.1 M PH 7.35; Tousimis). These samples were further fixed in 1% osmium–tetroxide (Electron Microscopy Sciences) for 2 h. Details of the sample preparation for imaging have been reported earlier.[34]

Photoacoustic FTIR

FTIR spectra were obtained on a Thermo Nicolet Nexus 870 spectrometer (Thermo Fisher Scientific, Waltham, MA, USA) which was equipped with a MTEC Model 300 photoacoustic (PA) accessory (MTEC Photoacoustics, Ames, IA, USA). The PA chamber was purged with dry helium for 15 min before collecting data for each sample. Spectra were all acquired in the range of 4000–400 cm^{-1}, with a spectral resolution of 4 cm^{-1}. GRAMS/32 software was utilized for spectra analysis. Second-derivative analysis determined the center positions for each sub-band in the curve-fitting. A Gaussian algorithm chose the shapes of the underlying bands.

XRD

XRD characterization was performed using an x-ray diffractometer (Philips Analytical X'pert MPD, Almelo, The Netherlands) with a secondary monochromator and Cu-tube by CuKα radiation wavelength of 1.5406 Å. XRD was conducted at a scan rate of 0.05°/s with the scan range of $2\theta = 20°$–60°. Transverse and longitudinal sections of healthy and OI bone samples were used for XRD characterization. The widths of the [002] profiles from all the samples were measured to obtain information on the size and/or internal perfection of the crystals along their *c*-axis. Assuming the changes in crystallinity result from size rather than strain effects, the crystal size of bone mineral can be obtained by using the Scherrer equation, $D = \lambda/\beta\cos\theta$, where D is the mean crystallite size, λ is the x-ray wavelength, θ is the Bragg angle, and β is the full width at half-maximum of the 002 profile expressed in radians.[35]

RESULTS

Microstructure of OI Human Cortical Bone

Healthy bone has a comparatively homogenous structure with well-attached mineralized fibrils.[36] In contrast, the structure of OI bone is quite different. Figure 2a–j shows the SEM images of the surfaces of the OI bone specimen fractured in liquid N_2. Loosely bound fibers and particles are observed on the OI bone surface (Fig. 2a and b, arrows), demonstrating a weaker interaction between the constituents of OI bone than those in healthy bone. Figure 2a and b also shows some osteons with good lamellae shapes; however, some have irregular and big Haversian canal channels (Fig. 2c and d, arrows) which can arise from abnormal remodeling processes. These significant porous structures intensify the fragility of the OI bone. Also, OI bone has abnormal collagen fiber areas

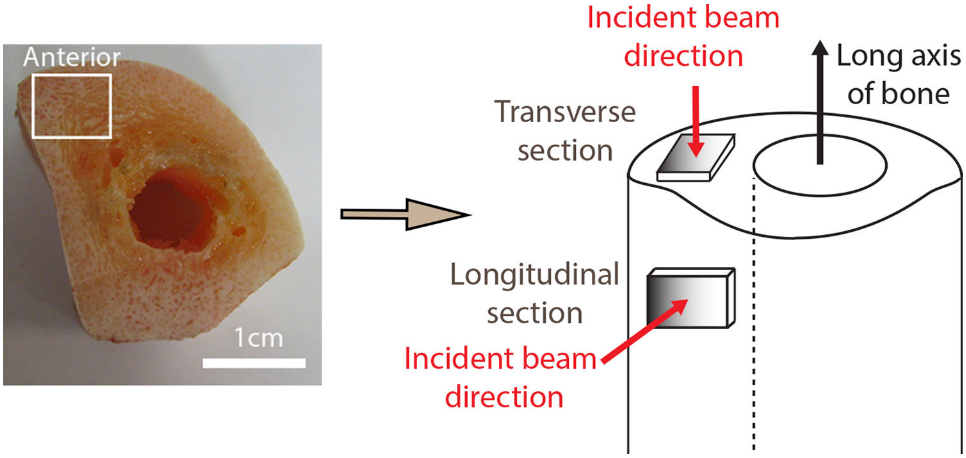

Fig. 1. Schematic representation of bone showing from where the samples were cut; transverse section and longitudinal section are both from the anterior area of OI bone specimen

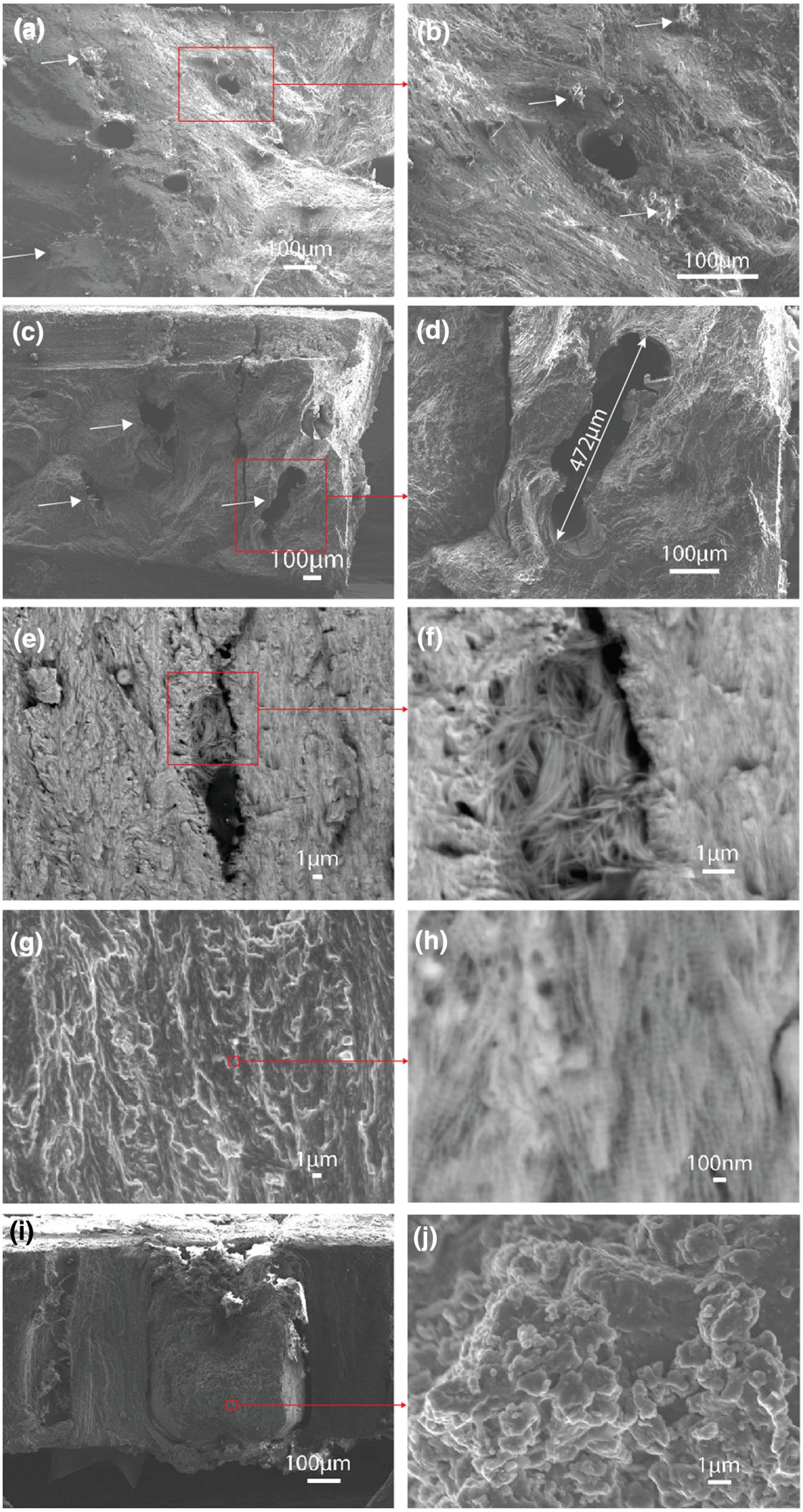
(a)
100µm
(b)
100µm
(c)
100µm
(d)
472µm
100µm
(e)
1µm
(f)
1µm
(g)
1µm
(h)
100nm
(i)
100µm
(j)
1µm

◀ Fig. 2. SEM micrographs of OI bone specimens. (b), (d), (f), (h) and (j) are the areas outlined in red in (a), (c), (e), (g) and (i), respectively, with higher magnification. In (a) and (b), arrows indicate loosely bound fibers and particles. In (c), arrows indicate big canals, and in (d), the maximum length of the canal is 472 μm. In (e) and (f), OI bone has abnormal collagen fiber areas within crevices. In (h), regular banding pattern was detected by the LABE detector on the normal area of OI bone specimen. However, the periodicity is different. In (i), an abnormal deposition of the mineral region with the size of about 485 μm × 629 μm as a separate cluster and the image at higher magnification (j) shows this area is overmineralized with globules of several microns.

within crevices (Fig. 2e and f). No banding pattern was observed on these abnormal collagen fibers using a low-angle backscattered electron (LABE) detector. In contrast, a regular banding pattern was detected by the LABE detector on the normal areas of the OI bone specimen (Fig. 2h). However, the periodicity of the banding pattern for the OI samples was measured to be about 62.0 nm on average which is smaller than the healthy bone periodicity of 67.0 nm. The OI bone specimen in this study also shows the abnormal deposition of the mineral region of size of about 485 μm × 629 μm as a separate cluster (Fig. 2i). The image at higher magnification (Fig. 2j) reveals that this area is overmineralized with globules of the size of several microns.

Comparison of Photoacoustic-FTIR (PA-FTIR) Spectra of Healthy and OI Bone

FTIR spectroscopy has been utilized to investigate healthy and diseased bones.[37] These spectroscopic techniques can reveal molecular information of materials regarding both composition and conformation. Due to the genetic mutants of procollagen molecules, an abnormal molecular structure of the protein in OI is expected. PA-FTIR spectra are shown in Fig. 3 for healthy and OI solid bone samples from the transverse and longitudinal sections in the energy range of 4000–400 cm^{-1}. These spectra were normalized using the O–H band (3322 cm^{-1}). The assignments of the bands are shown in Table I.[38–46]

The spectra shown in Fig. 3 indicate significant differences between healthy and OI bone specimens. For the organic component, C–H stretching bands around 2854 cm^{-1} and 2926 cm^{-1} and a C=O stretching band of OI bone exhibit much higher and sharper shapes than those of healthy bone,

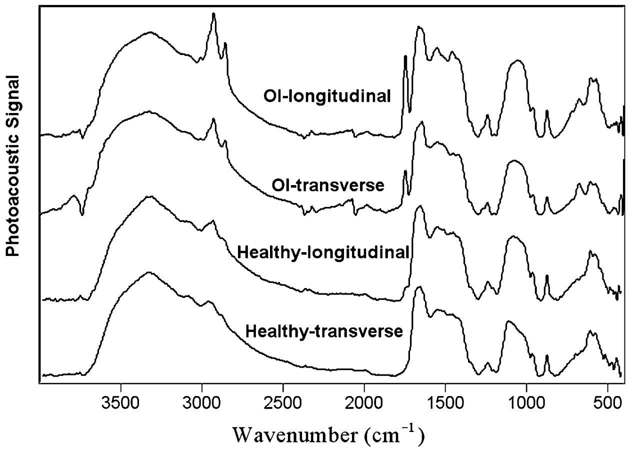

Fig. 3. PA-FTIR spectra of human OI cortical bone and healthy cortical bone (longitudinal and transverse sections, respectively) in the 4000–400 cm^{-1} region, velocity of mirror: 0.158 cm/s

Table I. Band assignments of PA-FTIR spectra from OI bone

Wavenumber (cm^{-1}) transverse	Wavenumber (cm^{-1}) longitudinal	Band assignment	References
3588	3588	Structural OH	38
3322	3322	OH stretching vibration from water and combination of Amide A with N–H stretching	39
3072	3074	Amide B Fermi resonance band of the first overtone of the Amide II band powered by N–H stretching vibration	40
2967	2965	CH_3 asymmetric stretch: mainly lipids	41
2925	2925	CH_2 asymmetric stretch: mainly lipids, with the little contribution from proteins, carbohydrates, nucleic acids	41
2856	2856	CH_2 symmetric stretch: mainly lipids, with the little contribution from proteins, carbohydrates, nucleic acids	41
2074, 1984	2076, 1983	OH stretching vibrations from P–OH	42–44
1746	1747	C=O stretch: lipids, cholesterol esters, triglycerides	45
~1652	~1652	Amide I (protein C=O stretch)	45
1551–1505	1550–1506	Amide II (protein N–H bend, C–N stretch)	45
1455, 1414	1457, 1413	CH_3 and carbonate v_3 vibration	41
1342	1342	CH_2 wagging	39
~1241	~1241	Amide 3(C–N stretch, N–H bend, C–C stretch)	39
1180–927	1180–927	v_3 PO_4^{3-}	39
875	875	v_2 CO_3^{2-}	39
640–710	640–710	C–S stretching vibration	46
607, 573	608, 570	v_4 PO_4^{3-}	39

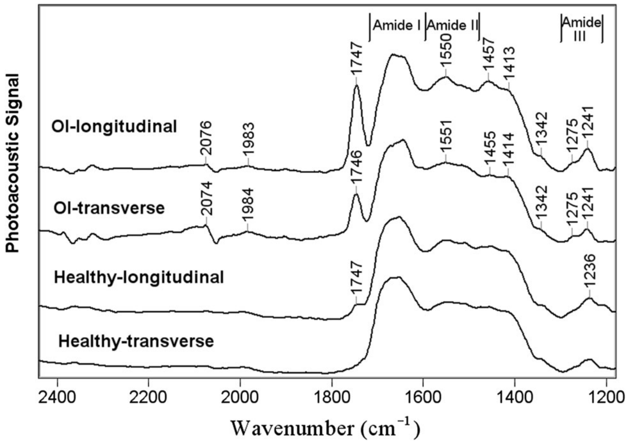

Fig. 4. PA-FTIR spectra of human OI cortical bone and healthy cortical bone (longitudinal and transverse sections, respectively) in the 2400–1180 cm^{-1} region.

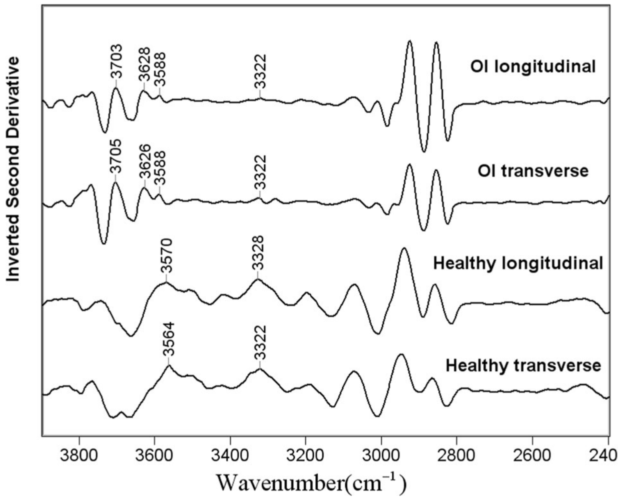

Fig. 5. Inverted second-derivative curves of FTIR spectra of healthy and OI bone in the energy range of 2400–3900 cm^{-1}.

whereas the band position remains the same, which suggests that their compositions are not noticeably abnormal. These bands around 2854 cm^{-1} and 2926 cm^{-1} are attributed to organic components such as lipids, proteins, carbohydrates and nucleic acids, while the band at 1747 cm^{-1} is assigned to lipids, cholesterol esters and triglycerides. The intensity differences in these bands indicate that this OI bone specimen contains relatively more non-collagenous organic components (as compared to collagen) than the healthy bone specimen. Also, a new prominent broad band emerges at around 640–710 cm^{-1} in the OI bone spectra. This band is assigned to the C–S stretching vibration[46] and the appearance of this new C–S band implies that the collagen molecules or other organic matrix components of the OI tibia may contain more cysteine. Since collagen molecules occupy 90% of all organic components in bone, the relatively high intensity of this new band is most likely from the type I collagen molecules. Therefore, the structure of collagen molecules may possess more cysteine replacement for glycine. The increased intensity of the band suggests that another possibility of relatively higher concentration of osteonectin, a cysteine-rich phosphorylated glycoprotein, is present in the OI sample.

The amide I, II, and III bands are major bands of collagen molecules. As seen from Fig. 4, amide I (protein C=O stretch, at around 1652 cm^{-1}) bands of the two sections of healthy bone are similar; however, they are different from those of OI bone. Although overlapped with the OH bending vibration, the amide I band profiles of OI bone are different, exhibiting significantly altered collagen structures. The bands of amide II (protein N–H bend, C–N stretch) at around 1546–1506 cm^{-1}, CH_3 and carbonate $\nu3$ vibrations at around 1457 cm^{-1} and 1413 cm^{-1}, respectively, are not prominent; therefore, they do not show the apparent difference between healthy and OI bone specimens. In contrast, the amide III (C–N stretch, N–H bend, C–C stretch) band of healthy bone is apparently different from that of OI bone: a band at around 1200 cm^{-1} in the healthy bone spectra almost disappears in the OI bone spectra; the peak of amide III in the OI spectra is at 1241 cm^{-1}, 5 cm^{-1} upshifting from that peak in the healthy bone spectra; and a small band at 1275 cm^{-1} appears in the OI bone spectra. The band of amide III provides both composition and secondary structure information of proteins. Therefore, it is too complex to analyze, but still reflects the significant alteration of the organic component of OI bone from healthy bone.

For the mineral component, the bands at 3073 cm^{-1} and 3628 cm^{-1} from the OI second-derivative spectral curve (Fig. 5) are assigned to the OH asymmetric stretching mode ($\nu3$), and the symmetric stretching mode ($\nu1$) for water associated with HAP.[38] The appearance of these new bands in the OI spectra indicates that water interacts more closely with HAP in the OI bone specimen as compared to healthy bone. The band at 3588 cm^{-1} in OI spectra, the stretching vibration of the structural hydroxyl group from HAP,[38] shifts to the higher energy side as compared to the band at 3570 cm^{-1} in healthy bone spectra, implying that the molecular structure of OI HAP is different from the healthy bone. The bands at around 2100 cm^{-1}, OH stretching vibrations from P–OH,[34] are more prominent in OI bone than in healthy bone, also implying differences between normal and OI bone minerals. Unlike synthetic HAP, the HAP present in human bone is calcium-deficient and contains specific lattice substitutions such as CO_3^{2-} and HPO_4^{2-} species, and ion vacancies in the apatitic crystals.[47] Since P–OH originates from HPO_4^{2-}, the stronger appearance of the OH stretching vibrations from the P–OH of OI bone implies that OI bone contains more HPO_4^{2-} than healthy bone.

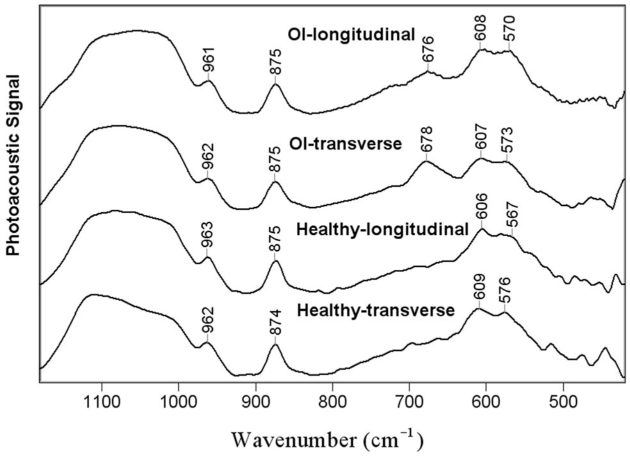

Fig. 6. PA-FTIR spectra of human OI cortical bone and healthy cortical bone (longitudinal and transverse sections, respectively) in the 1180–420 cm^{-1} region.

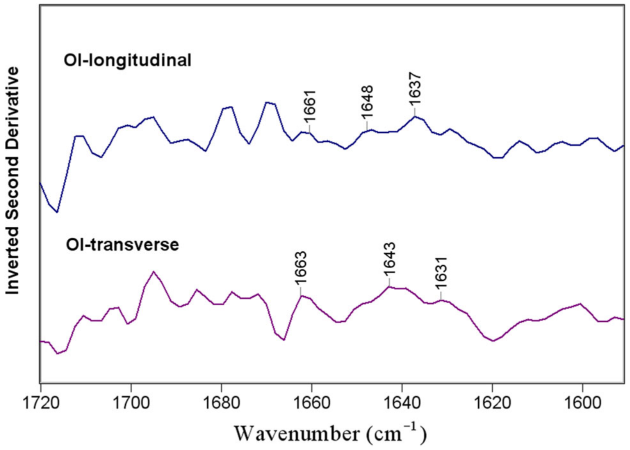

Fig. 7. Inverted second-derivative curves of FTIR spectra of OI longitudinal and transverse sections in the 1720–1590 cm^{-1} region.

The $\nu4$ PO_4^{3-} band at 572–610 cm^{-1} of the two bone specimens appears similar, as shown in Fig. 6. However, the broad profiles of the $\nu3\nu1$ PO_4^{3-} band at 1180–927 cm^{-1} differ from one another. The $\nu2$ out-of-plane bending vibration of CO_3^{2-} at 873 cm^{-1} retains the same position and shape. However, the ratio of its intensity over the $\nu3\nu1$ PO_4^{3-} band is lower in OI bone than in healthy bone, indicating that CO_3^{2-} ions present in the OI mineral are reduced as compared to the mineral from the healthy specimen.

Comparison of PA-FTIR Spectra OI Bone in Transverse and Longitudinal Planes

The PA-FTIR spectra of the transverse and longitudinal sections of OI bone have also been compared, as seen in Fig. 3. The C–H stretching vibrations at around 2855 cm^{-1} and 2926 cm^{-1}, and the C=O stretching vibration at around 1747 cm^{-1} of the longitudinal section are more intense than those of the transverse section. This is also seen in healthy bone, possibly from more canals crosscut and exposed on the longitudinal section surface.[34] As mentioned before, the amide I (protein C=O stretch, at around 1652 cm^{-1}) band of OI bone differs from the healthy bone. The amide I band is overlapped by the O–H bending band from the water. Therefore, the orientational difference of the amide I band is not easily observed. However, in OI, the amide I band of the longitudinal section differs from that of the transverse section as can be seen in Fig. 7. The bands of amide II (protein N–H bend, C–N stretch) at around 1546–1506 cm^{-1}, and CH_3 and carbonate $\nu3$ vibrations at around 1457 cm^{-1} and 1413 cm^{-1}, respectively, are all more intense in the longitudinal section than in the transverse section. These effects have also been observed in the amide III band.

Further, the O–H stretching band from P–OH at around 2000 cm^{-1} from the transverse section is stronger than that of the longitudinal section, indicating that the transverse section contains more HPO_4^{2-} than the longitudinal section. From Fig. 3, more CO_3^{2-} ion content and less HPO_4^{2-} ion in the longitudinal sections than in the transverse sections are also observed. The broad profile of $\nu3\nu1$ PO_4^{3-} band at 1180–927 cm^{-1} arises from 12 sub-bands (Table II[48–50]). Curve fitting in this region is performed based on the second derivative of the curves with the normalization depicted in Fig. 8a and b. The ratio of the 1023/1038 cm^{-1} bands (often used to describe the relative amount of crystal perfection or the amount of non-stoichiometric apatite in the lattice)[32,48,51] in the transverse section is 0.45, while, in the longitudinal section, it is 0.21. Further, the sub-band area at around 1090 cm^{-1} (often used to describe the amount of stoichiometric apatite in the lattice)[32,48,51] in the longitudinal section is larger than that in the transverse section. Therefore, OI bone appears to be more stoichiometric in the longitudinal section surface. This phenomenon is the same as in healthy bone but at a different intensity.[34]

XRD and EDS Results

Usually, a sample of bone tissue contains crystals of very different ages and at varying stages of maturation. The ages and the stages of maturation are attributed to the length of time the individual crystals remain in the tissue, since the remodeling proceeds heterogeneously throughout life.[52] In this study, a piece of copper filter with a 10 mm × 1 mm window was used to focus the size of the beam on the samples. The mineral information acquired by XRD reflects an average from that size of bone tissue. XRD is sensitive to the long-range crystalline structure of the material.[53]

Figure 9 shows the x-ray diffraction profiles of healthy and OI bone specimens, with their transverse sections and longitudinal sections, respectively. The profiles show intensity peaks from (002), (211), (202), (310), (203), (213), and (004) planes. All

Table II. Major components of the $\nu1$, $\nu3$ PO_4^{3-} bands[48–50]

Position transverse	Area transverse	Position longitudinal	Area longitudinal	Band assignment
1160	6	1160	11	HPO_4^{2-} containing apatites
1120	134	1120	121	$\nu3$ PO_4^{3-} in poorly crystalline apatites
1107	14	1108	20	$\nu3$ PO_4^{3-} in poorly crystalline apatites
1090	36	1089	51	$\nu3$ PO_4^{3-} in stoichiometric HA
1075	23	1073	24	$\nu3$ PO_4^{3-} in poorly crystalline apatites
1061	62	1060	62	$\nu3$ PO_4^{3-} in poorly crystalline apatites
1045	39	1043	31	HPO_4^{2-} containing apatites and type B carbonate-containing apatites
1038	61	1036	63	PO_4^{3-} in stoichiometric HA
1022	28	1025	13	Non-stoichiometric apatites containing HPO_4^{2-} and/or CO_3^{2-}
1004	83	1005	97	$\nu3$ PO_4^{3-} in apatitic environment
1001	3	998	5	$\nu3$ PO_4^{3-} in apatitic environment
959	26	959	33	$\nu1$ PO_4^{3-}

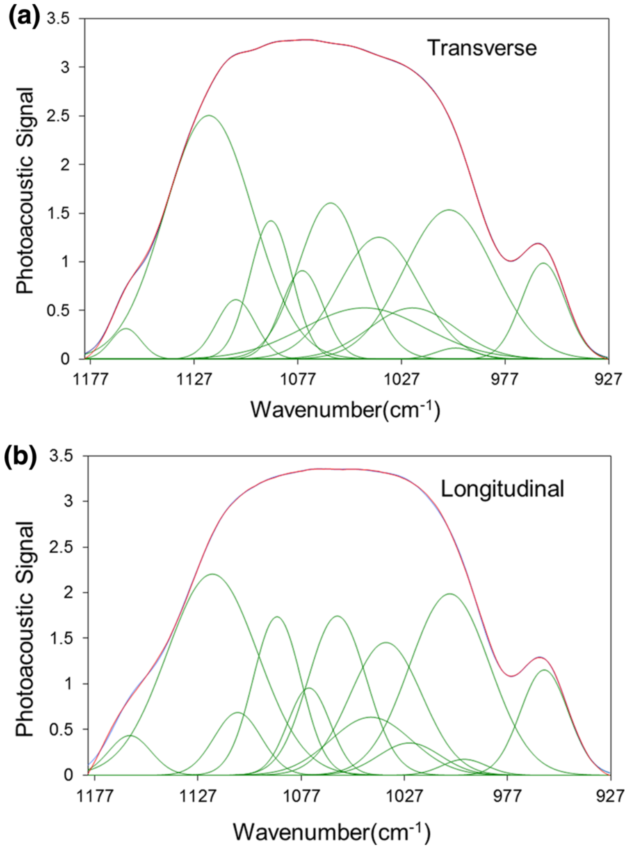

Fig. 8. Curve fitting analysis of the $\nu1$ and $\nu3$ phosphate bands (1180–927 cm^{-1}) of (a) transverse section, and (b) longitudinal sections of bone specimens.

the profiles are normalized at the strongest peak of (211) reflection. As compared to the well-crystallized HAP,[54] all x-ray lines of bone specimens are broadened except the (002) reflection. The x-ray line broadening results primarily from the smaller crystallite size (<200 nm) and lattice strain or crystal distortions resulting from atomic substitutions within the crystal lattice. The (211) broad profile is overlapped with (112), (300), and (202) reflections.[55] The (002) reflection is the only one free of any overlapping adjacent lines. This (002) reflection reflects the length axis of the bone crystal with minimal strain influence. The aging-related effects on crystallite size[55] are expected to be minimal in the current samples, and disease is the only influencing issue. The Scherrer equation was used to obtain crystal sizes along the *c*-axis direction of healthy and OI bone specimens which are listed in Table III. The crystal sizes along the *c*-axis direction of healthy bone in the transverse and longitudinal sections are calculated as 28.35 nm and 25.82 nm, whereas the crystal sizes of OI bone in the transverse and longitudinal sections are 28.42 nm and 20.80 nm, respectively. The crystal sizes of the two transverse sections are the largest among all the specimens, and they are very close. The largest observed difference is between the two longitudinal sections. Since the *c*-axis is perpendicular to the transverse section plane, the signals from the transverse sections are much stronger than the longitudinal section. The (002) plane also shows orientational difference; the transverse section is more intense in both healthy and OI bone specimens than the longitudinal section. Overall, the crystal size along the *c*-axis direction of OI bone is close to healthy bone, implying that OI and healthy bone have similar-sized mineral crystals. As seen in Table IV, the Ca/P molar ratio of healthy and OI bone specimens obtained from EDS are found to be similar.

DISCUSSION

Even in severe OI cases, there are normal lamellar bone structures observed that are composed of normally mineralized fibrils.[36] In the present study, FE-SEM images show some normal lamellae. Meanwhile, these images also reveal significantly altered structures of OI bone from healthy bone on all scales, e.g., OI bone is more porous and fibrous, and

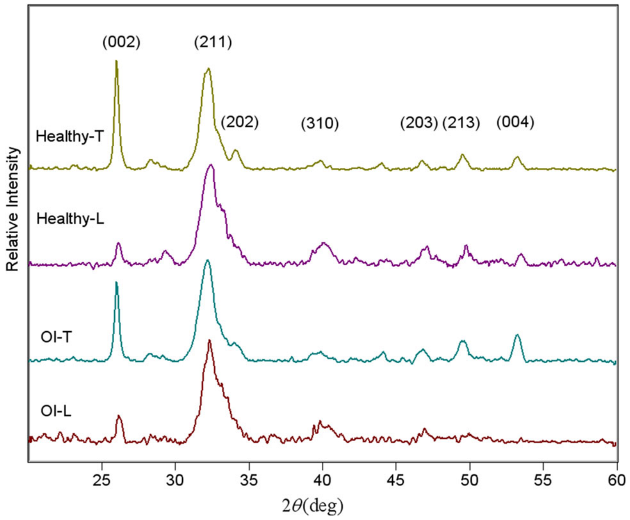

Fig. 9. X-ray diffractogram of bone specimens: Healthy bone (T-transverse section and L-longitudinal section) and OI bone specimens.

Table III. Crystal size along *c*-axis direction of bone mineral (nm)

	Transverse section	Longitudinal section
Healthy bone	28.35	25.82
OI bone	28.42	20.80

Table IV. Ca/P molar ratio of bone specimens (±STD)

	Transverse section	Longitudinal section
Healthy bone	1.53 ± 0.06	1.41 ± 0.09
OI bone	1.46 ± 0.02	1.42 ± 0.02

OI bone contains abnormal collagen fibril areas and overmineralized deposits, and an abnormal banding pattern of mineralized fibrils. The changes in bone porosity at the tissue level indicate changes in bone metabolism and altered bone mechanical integrity. The loosely attached fibrils and condensed mineral areas are the signs of weakened intermolecular adhesion and interaction between collagen molecules and mineral phase. The abnormal banding pattern of mineralized fibrils demonstrates the influence of the poor collagen matrix, which serves as a framework for biomineralization. It seems that the entire bone structure as seen in SEM images is significantly altered due to the collagen defects and secondary changes caused by the collagen defects.

PA-FTIR spectra display aberrant structures of collagen molecules and slightly altered minerals. According to the FTIR analysis of the organic components, the C–H stretching bands and C=O stretching bands from the non-collagenous organic components remain in their same positions in the OI spectra as in the healthy bone spectra, implying that the main compositions of the non-collagenous organic components are not noticeably abnormal. However, the volume of the non-collagenous organic components is relatively greater because of their higher intensity. This can result from the porous feature of the OI bone which can accommodate more non-collagenous proteins (NCPs). In a previous study, the amount of total protein synthesized by osteoblasts from patients with mild to moderately severe forms of OI was found to be normal when compared to that of an age-matched control.[4] The increased levels of NCPs in OI bone reflect a reduced collagen content.[56] This viewpoint accords with the present FTIR results. The collagen molecules of OI bone have altered structures due to the apparently altered amide I and amide III bands. Also, the appearance of a new band at 705–640 cm^{-1} implies that more cysteine may be contained in the collagen molecules as substitutions, and more likely from higher concentrations of osteonectin (a cysteine-rich phosphorylated glycoprotein) present in OI tibia. Osteonectin was found to be reduced in bones from OI patients as compared with age-matched normal controls.[4,56] However, as seen from the figure in Ref. [4] the amount of collagen from OI type I is about 20% of that of age-matched normal controls, while the amount of osteonectin from OI type I is about 60% of that of age-matched normal controls. Therefore, as compared with collagen, osteonectin is increased in OI type I bone.

The mineral component shows three different kinds of OH stretching bands between OI and healthy bones. The first kind of OH stretching bands shows two new bands at 3703 cm^{-1} and 3628 cm^{-1}, and their appearance indicates that water interacts more closely with HAP in OI bone specimens. A 12-cm^{-1} upshifting of the stretching vibration of the structural hydroxyl group from hydroxyapatite implies that the molecular structure of OI hydroxyapatite is slightly different from healthy bone. Also, around 2000 cm^{-1}, bands of OH stretching vibrations from P–OH of OI bone are more prominent than in healthy bone, indicating that OI bone may contain more HPO_4^{2-} ions. This agrees with a previous study that demonstrated increased acid phosphate content in Brtl/ + teeth.[33] In contrast to the OH stretching bands, the intensity ratio of $\nu 2$ CO_3^{2-} over $\nu 3 \nu 1$ PO_4^{3-} bands in OI is lower than in healthy bone, indicating less CO_3^{2-} ions in OI mineral. This lower CO_3^{2-}/PO_4^{3-} ratio has also been found in several OI bone studies.[12,13] However, PO_4^{3-} and CO_3^{2-} bands of OI bone do not display significant differences as compared to healthy bone. Therefore, in OI, the mineral component does not have significant molecular alterations. Our XRD and EDS results on both healthy and OI bone specimens also support that the mineral crystals in OI are not significantly altered. Studies of phosphorus-31 solid state nuclear magnetic resonance (^{31}P-NMR) spectra also suggest that the bulk of the phosphorus in both healthy and OI samples are present in the same phase.[15] In another study, it has been reported that the monovalent ion OH^- within the apatite tunnels can be easily exchanged at high temperatures without any crystal alteration, whereas the trivalent ion PO_4^{3-} and bivalent ion Ca^{2+} that constitute the apatite frame can be substituted, but with structure reorganization.[57] Therefore, in OI, there are alterations of the OH^- groups, but these alterations do not remarkably influence the whole crystal structure. Instead, they change the mineral ion environment, making it more attachable to water and elevating the number of HPO_4^{2-} ions in the hydrated layer of the mineral crystal. The improved attaching ability of OI bone mineral to water and the non-stoichiometry of the mineral favor the resorption of bone by osteoclasts.

FTIR spectra exhibit increased CO_3^{2-} ion content and reduced HPO_4^{2-} ion content in healthy bone compared with in OI bone, implying that healthy bone is more mature than OI bone, which also suggests that healthy bone is more stoichiometric. Previously, ^{31}P-NMR spin–spin relaxation studies[58] have shown that a substantial fraction of the protonated phosphates (HPO_4^{2-}) are situated on the surfaces of the bone mineral crystals, and that the concentration of unprotonated phosphates (PO_4^{3-}) within the apatitic lattice increases toward the center of the crystal. In more mature bone, the mineral is more stoichiometric.[48,52,59] In a previous work,[34] it was reported that longitudinal section is more stoichiometric. This phenomenon is attributed to the reduced interaction between exchangeable ions contained within the mineral surface and collagen molecules in the longitudinal section rather than the interaction between the mineral surface and collagen termini in the transverse section. Therefore, the non-stoichiometry of OI bone mineral is possibly influenced by the interactions between the collagen and mineral. The 1020 cm^{-1}/1030 cm^{-1} band ratio has long been regarded as the measure of the “crystallinity/maturity index” of bone mineral, and the more crystalline/mature, the more hydroxyapatite-like stoichiometry, the bigger the crystalline size, and the less the ion substitution by ions such as CO_3^{2-}.[50,51]

The FTIR spectra also indicate higher CO_3^{2-} ion content and less HPO_4^{2-} ion content in the longitudinal section of OI bone than in the transverse section, implying that the longitudinal section is more stoichiometric for the same reason as previously discussed. Since the crystalline HAP core is stoichiometric, the non-stoichiometric ions and vacancies are located on the mineral surface as the hydrated layer. The transverse section is more non-stoichiometric, implying that the hydrated layer in the transverse plane has a greater volume than it does in the longitudinal plane. This schematic nanocrystal of bone mineral is illustrated in Fig. 10. It is commonly accepted that the biomineralization process is controlled by bone cells and interactive non-collagenous phosphorylated proteins, and is also influenced by collagen.[60] Osteoblast cells derived from OI patients are found to have reduced levels of collagen, osteonectin and three proteoglycans (a large chondroitin sulfate proteoglycan, biglycan, and decorin), and elevated amounts of thrombospondin and fibronectin when compared with levels found in age-matched control bone cell cultures.[4,61] In another study, osteonectin was found to be reduced in the bone of all OI patients, with the lowest levels from severely affected type III OI patients.[56] These alterations in NCPs give rise to an extracellular matrix with an aberrant stoichiometry.[4] In the present study, osteonectin is quite possibly the source of the C–S band at around 640–710 cm^{-1} from OI bone. The relative higher amount of osteonectin as compared to collagen is likely the cause of the high mineralization of OI bone. Except for the probable abnormal amount of osteonectin, the overall composition of NCPs in OI do not show remarkable changes as compared to the healthy bone in IR spectra, and the crystal structure and Ca/P ratio as investigated by XRD and EDS do not have significant differences between OI and healthy bones. Conversely, collagen molecules are significantly altered. Therefore, the experiments reported also suggest that the biomineralization process is more controlled by NCPs than collagen with a prominent role of water molecules.

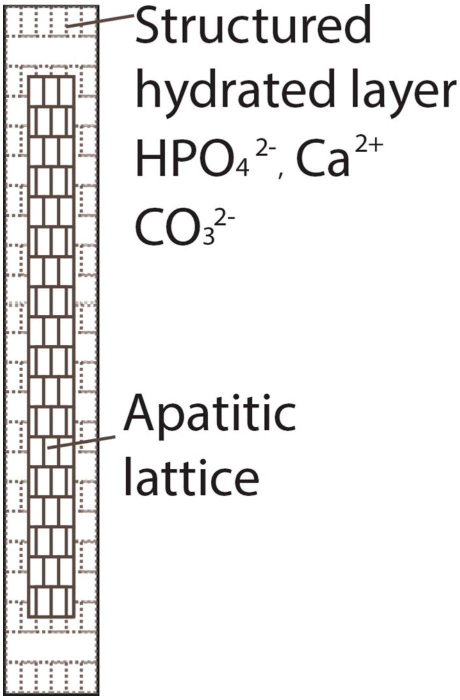

Fig. 10. Schematic showing structure of an HAP nanocrystal in bone.

CONCLUSION

With OI disease, the mutations in procollagen molecules cause aberrant collagen molecules and secondary changes in mineral, NCPs, and cell activities due to their interactions and cross-talk with collagen matrix. In the present study, FE-SEM, PA-FTIR, XRD, and EDS have been utilized to characterize the OI human cortical bone (putative type I) and healthy human cortical bone. The study demonstrates that OI bone structure is significantly altered due to collagen defects. FE-SEM images show more porous, fibrous features, abnormal collagen fibrils, overmineralized deposits, and an altered banding pattern of mineralized fibrils of OI bone. PA-FTIR spectra demonstrate altered OI collagen molecules with a markedly different amide III band, and the appearance of a new C–S band can result from a combination of collagen defect (cysteine replacement of glycine) and an increased amount of osteonectin (a cysteine-rich phosphorylated glycoprotein). A slightly altered mineral structure and more HPO_4^{2-} in OI is also seen in the spectra. PA-FTIR spectra also show that OI bone mineral is more attachable to water and is more non-stoichiometric than healthy bone, arising from the altered mineral ion environment. The loosely attached fibrils and condensed mineral areas are the results of weakened intermolecular adhesions and poor collagen frameworks. The banding pattern of mineralized fibrils is slightly altered in OI because of the altered collagen framework. OI bone has the same orientational stoichiometry of hydroxyapatite as healthy cortical bone; that is, the longitudinal section is more stoichiometric than the transverse section. This orientational stoichiometry results from the interaction between the mineral surface and the different parts of collagen molecules as discussed in our previous study.[34] A larger volume of the hydrated layer in the transverse plane of the bone mineral nanocrystal is also suggested.

ACKNOWLEDGEMENTS

Instrumentation obtained from National Science Foundation MRI grants is acknowledged for enabling experiments conducted in this work. The authors would like to acknowledge the assistance in electron microscopy laboratory from Mr. Scott Payne. Author CG would like to acknowledge the support from Doctoral Dissertation Award of NDSU graduate school.

REFERENCES

1. F. Rauch and F.H. Glorieux, *Lancet* 363, 1377 (2004).
2. B. Sykes, D. Ogilvie, P. Wordsworth, G. Wallis, C. Mathew, P. Beighton, A. Nicholls, F.M. Pope, E. Thompson, P. Tsipouras, R. Schwartz, O. Jensson, A. Arnason, A.L. Borresen, A. Heiberg, D. Frey, and B. Steinmann, *Am. J. Hum. Genet.* 46, 293 (1990).
3. F.S.V. Dijk, J.M. Cobben, K.A.A. Maugeri, P.G.J. Nikkels, R.R.V. Rijn, and G. Pals, *Mol. Syndromol.* 2, 1 (2011).
4. N. Fedarko, U. Vetter, and P. Robey, *Connect. Tissue Res.* 31, 269 (1995).
5. S.L. Teitelbaum, W.J. Kraft, R. Lang, and L.V. Avioli, *Calc. Tissue Res.* 17, 75 (1974).
6. T.J. Sims, C.A. Miles, A.J. Bailey, and N.P. Camacho, *Connect. Tissue Res.* 44, 202 (2003).
7. J.P. Cassella, P. Barber, A.C. Catterall, and S.Y. Ali, *Bone* 15, 329 (1994).
8. P. Sarathchandra, F.M. Pope, and S.Y. Ali, *Calcif. Tissue Int.* 65, 390 (1999).
9. N.S. Fedarko, P.G. Robey, and U.K. Vetter, *J. Bone Miner. Res.* 10, 1122 (1995).
10. N.S. Fedarko, P.D. Sponseller, and J.R. Shapiro, *J. Bone Miner. Res.* 11, 800 (1996).
11. W.J. Grzesik, C.R. Frazier, J.R. Shapiro, P.D. Sponseller, P.G. Robey, and N.S. Fedarko, *J. Biol. Chem.* 277, 43638 (2002).
12. N.P. Camacho, W.J. Landis, and A.L. Boskey, *Connect. Tissue Res.* 35, 259 (1996).
13. N.P. Camacho, L. Hou, T.R. Toledano, W.A. Ilg, C.F. Brayton, C.L. Raggio, L. Root, and A.L. Boskey, *J. Bone Miner. Res.* 14, 264 (1999).
14. R.M. Coleman, L. Aguilera, L. Quinones, L. Lukashoya, C. Poirier, and A. Boskey, *Bone* 51, 920 (2012).
15. J.P. Cassella, P.J. Barrie, N. Garrington, and S.Y. Ali, *J. Bone Miner. Metab.* 18, 291 (2000).
16. R. Baron, J.M. Gertner, R. Lang, and A. Vignery, *Pediatr. Res.* 17, 204 (1983).
17. F. Rauch, R. Travers, A.M. Parfitt, and F.H. Glorieux, *Bone* 26, 581 (2000).
18. I. Kalajzic, J. Terzic, Z. Rumboldt, K. Mack, A. Naprta, F. Ledgard, G. Gronowicz, S.H. Clark, and D.W. Rowe, *Endocrinology* 143, 1594 (2002).
19. E.F. McCarthy, K. Earnest, K. Rossiter, and J. Shapiro, *Clin. Orthop. Relat. R.* 336, 254 (1997).
20. A.M. Lund, M. Hansen, G. Kollerup, A. Juul, B. Teisner, and F. Skovby, *Acta Paediatr.* 87, 1131 (1998).
21. J.P. Cassella, T.C.B. Stamp, and S.Y. Ali, *Calcif. Tissue Int.* 58, 155 (1996).
22. P. Sarathchandra, F.M. Pope, M.V. Kayser, and S.Y. Ali, *J. Pathol.* 192, 385 (2000).
23. P. Roschger, N. Fratzl-Zelman, B.M. Misof, F.H. Glorieux, K. Klaushofer, and F. Rauch, *Calcif. Tissue Int.* 82, 263 (2008).
24. F. Rauch, L. Lalic, P. Roughley, and F.H. Glorieux, *J. Bone Miner. Res.* 25, 1367 (2010).
25. C. Gu, D.R. Katti, and K.S. Katti, *Bioinspired Biomim. Nanobiomater.* 4, 15 (2015).
26. K.S. Katti, C. Gu, and D.R. Katti, *Biomech. Model Mechan.* (2015). doi:10.1007/s10237-015-0727-4.
27. N. Wasserman, J. Yerramshetty, and O. Akkus, *Eur. J. Morphol.* 42, 43 (2005).
28. A. Carriero, E.A. Zimmermann, A. Paluszny, S.Y. Tang, H. Bale, B. Busse, T. Alliston, G. Kazakia, R.O. Ritchie, and S.J. Shefelbine, *J. Bone Miner. Res.* 29, 1392 (2014).
29. K. Lindahl, A.M. Barnes, N. Fratzl-Zelman, M.P. Whyte, T.E. Hefferan, E. Makareeva, M. Brusel, M.J. Yaszemski, C.-J. Rubin, A. Kindmark, P. Roschger, K. Klaushofer, W.H. McAlister, S. Mumm, S. Leikin, E. Kessler, A.L. Boskey, O. Ljunggren, and J.C. Marini, *Hum. Mutat.* 32, 598 (2011).
30. R. Bogan, R.C. Riddle, Z. Li, S. Kumar, A. Nandal, M.-C. Faugere, A. Boskey, S.E. Crawford, and T.L. Clemens, *J. Bone Miner. Res.* 28, 1531 (2013).
31. N.P. Camacho, P. Carroll, and C.L. Raggio, *Calcif. Tissue Int.* 72, 604 (2003).
32. L. Spevak, C.R. Flach, T. Hunter, R. Mendelsohn, and A. Boskey, *Calcif. Tissue Int.* 92, 418 (2013).
33. A.L. Boskey, K. Verdelis, L. Spevak, L. Lukashova, E. Beniash, X. Yang, W.A. Cabral, and J.C. Marini, *BioMed Res. Int.* 2013, 295812 (2013).
34. C. Gu, D.R. Katti, and K.S. Katti, *Spectrochimica Acta A Mol. Biomol Spectrosc.* 103, 25 (2013).
35. U. Vetter, E.D. Eanes, J.B. Kopp, J.D. Termine, and P.G. Robey, *Calcif. Tissue Int.* 49, 248 (1991).
36. W. Traub, T. Arad, U. Vetter, and S. Weiner, *Matrix Biol.* 14, 337 (1994).

37. A. Boskey and R. Mendelsohn, *J. Biomed. Opt.* 10, 031102 (2005).
38. J. Reyes-Gasga, R. Garcia-Garcia, M.J. Arellano-Jimenez, E. Sanchez-Pastenes, G.E. Tiznado-Orozco, I.M. Gil-Chavarria, and G. Gomez-Gasga, *J. Phys. D-Appl. Phys.* 41, 225407 (2008).
39. N. Kourkoumelis and M. Tzaphlidou, *Thescientificworldjo.* 10, 402 (2010).
40. W.H. Moore and S. Krimm, *Biopolymers* 15, 2439 (1976).
41. S. Garip and F. Severcan, *J. Pharm. Biomed.* 52, 580 (2010).
42. Z.H. Cheng, A. Yasukawa, K. Kandori, and T. Ishikawa, *Langmuir* 14, 6681 (1998).
43. E. Bertoni, A. Bigi, G. Cojazzi, M. Gandolfi, S. Panzavolta, and N. Roveri, *J. Inorg. Biochem.* 72, 29 (1998).
44. R. Kumar, K.H. Prakash, P. Cheang, L. Gower, K.A. Khor, and J.R. Soc, *Interface* 5, 427 (2008).
45. K. Singh, K.S. Lee, D. Lee, Y.K. Kim, and K.C. Kim, *J. Mech. Sci. Technol.* 24, 1661 (2010).
46. G. Socrates, *Infrared and Raman Characteristic Group Frequencies: Tables and Charts*, 3rd ed. (Chichester: Wiley, 2004).
47. D. Farlay, G. Panczer, C. Rey, P.D. Delmas, and G. Boivin, *J. Bone Miner. Metab.* 28, 433 (2010).
48. E.P. Paschalis, E. DiCarlo, F. Betts, P. Sherman, R. Mendelsohn, and A.L. Boskey, *Calcif. Tissue Int.* 59, 480 (1996).
49. D. Magne, P. Weiss, J.M. Bouler, O. Laboux, and G. Daculsi, *J. Bone Miner. Res.* 16, 750 (2001).
50. C. Rey, M. Shimizu, B. Collins, and M.J. Glimcher, *Calcif. Tissue Int.* 49, 383 (1991).
51. E.P. Paschalis, F. Betts, E. DiCarlo, R. Mendelsohn, and A.L. Boskey, *Calcif. Tissue Int.* 61, 480 (1997).
52. C. Rey, A. Hina, A. Tofighi, and M.J. Glimcher, *Cell Mater.* 5, 345 (1995).
53. B. Wopenka and J.D. Pasteris, *Mat. Sci. Eng. C-Biomim.* 25, 131 (2005).
54. R.A. Harper, A.S. Posner, and P. Soc, *Exp. Biol. Med.* 122, 137 (1966).
55. R.G. Handschin and W.B. Stern, *Bone* 16, S355 (1995).
56. U. Vetter, L.W. Fisher, K.P. Mintz, J.B. Kopp, N. Tuross, J.D. Termine, and P.G. Robey, *J. Bone Miner. Res.* 6, 501 (1991).
57. S. Cazalbou, C. Combes, D. Eichert, and C. Rey, *J. Mater. Chem.* 14, 2148 (2004).
58. Y.T. Wu, J.L. Ackerman, H.M. Kim, C. Rey, A. Barroug, and M.J. Glimcher, *J. Bone Miner. Res.* 17, 472 (2002).
59. C. Rey, V. Renugopalakrishnan, B. Collins, and M.J. Glimcher, *Calcif. Tissue Int.* 49, 251 (1991).
60. A. George and A. Veis, *Chem. Rev.* 108, 4670 (2008).
61. N.S. Fedarko, M. Moerike, R. Brenner, P.G. Robey, and U. Vetter, *J. Bone Miner. Res.* 7, 921 (1992).